Topographic gravity modelling for global Bouguer maps to degree 2,160: Validation of spectral and spatial domain forward modelling techniques at the 10 microgal level

Christian Hirt[1,2]*, Elisabeth Reußner[1], Moritz Rexer[1,2] and Michael Kuhn[3]

[1]Institute for Astronomical and Physical Geodesy,
Technische Universität München, Germany

[2]Institute for Advanced Study,
Technische Universität München, Germany

[3]Western Australian Geodesy Group & The Institute for Geoscience Research,
Curtin University, GPO Box U1987, Perth, WA 6845, Australia

* Corresponding author, Email: c.hirt@tum.de

Key points

- Complete spectral modelling of gravity field implied by degree-2160 topography
- Spatial and spectral gravity forward-modelling techniques to agree at 10 microgal level
- First successful validation of new degree-2160 spherical harmonic Bouguer gravity maps

Abstract

Over the past years, spectral techniques have become a standard to model Earth's global gravity field to 10 km scales, with the EGM2008 geopotential model being a prominent example. For some geophysical applications of EGM2008, particularly Bouguer gravity computation with spectral techniques, a topographic potential model of adequate resolution is required. However, current topographic potential models have not yet been successfully validated to degree-2160, and notable discrepancies between spectral modelling und Newtonian (numerical) integration well beyond the 10 mGal-level have been reported.

Here we accurately compute and validate gravity implied by a degree-2160 model of Earth's topographic masses. Our experiments are based on two key strategies, both of which require advanced computational resources. First, we construct a spectrally complete model of the gravity field which is generated by the degree-2160 Earth topography model. This involves expansion of

the topographic potential to the 15th integer power of the topography and modelling of short-scale gravity signals to ultra-high degree of 21,600, translating into unprecedented fine scales of 1 km. Second, we apply Newtonian integration in the space-domain with high spatial resolution to reduce discretisation errors.

Our numerical study demonstrates excellent agreement (8 microgal RMS) between gravity from both forward modelling techniques, and provides insight into the convergence process associated with spectral modelling of gravity signals at very short scales (few km). As key conclusion, our work successfully validates the spectral-domain forward modelling technique for degree-2160 topography, and increases the confidence in new high-resolution global Bouguer gravity maps.

Key words: Gravity, Bouguer gravity, topography, gravity forward modelling, topographic potential

1. Introduction

The Bouguer gravity anomaly, i.e., observed gravity reduced for the gravitational attraction generated by the topographic masses, plays a key role in geophysical studies of interior mass variations associated with geological units [e.g., *Jacoby and Smilde,* 2009]. The gravitational attraction of the topographic masses (short: topographic gravity, also denoted as gravity effect or Bouguer reduction in the literature) is usually computed from digital terrain models via some form of Newton's integral. Gravity computation techniques - commonly known as gravity forward modelling - can be grouped into two categories, namely spatial-domain and spectral-domain techniques [e.g., *Nahvandchi,* 1999; *Kuhn and Seitz,* 2005; *Hirt and Kuhn,* 2014]. In the first category, Newton's integral is evaluated in the space domain, e.g., through numerical integration using elementary mass bodies [*Kuhn et al*., 2009; *Grombein et al.* 2016], fast fourier transform (FFT)-techniques [*Forsberg,* 1984], or quadrature-based methods [*Hwang et al.,* 2003]. Classical [e.g., *Hammer,* 1939; *Nowell,* 1999] and modern [e.g., *Tsoulis et al.,* 2009; *Cella,* 2015] terrain correction computations fall into this category, too.

The second category comprises all methods that evaluate Newton's integral in the spectral domain [e.g., *Rummel et al.,* 1988; *Balmino,* 1994; *Wieczorek and Phillips,* 1998; *Tenzer,* 2005; *Balmino et al.,* 2012; *Gruber et al.,* 2014; *Rexer et al.,* 2016]. This involves spherical-harmonic expansion of the topographic gravitational potential (short: topographic potential) into higher-order integer powers of the global topography and calculation of topographic gravity through synthesis techniques [e.g., *Hirt and Kuhn,* 2012].

While spatial-domain techniques are usually applied for the Bouguer reduction of local or regional gravity surveys [e.g., *Jacoby and Smilde,* 2009], spectral-domain techniques are particularly well-suited for the computation of Bouguer gravity anomalies on a global scale. Due to their "global nature", spectral techniques inherently deliver the gravitational attraction of the global topographic masses. This also includes the effect of remote masses that are neglected in conventional Bouguer gravity maps [cf. *Kuhn et al*., 2009].

Global Bouguer gravity maps, obtained as difference of gravity effects from (a) a global gravitational model (GGM) and (b) a topographic potential model have become increasingly popular in the geoscience community: Bouguer maps have been constructed and used for Earth, e.g., based on the GOCE [*Pail et al.,* 2011] gravity satellite mission data to harmonic degree ~280 [cf. *Rexer et al., 2015*; *Braitenberg et al.,* 2015], from the EGM2008 [*Pavlis et al.,* 2008, 2012] model to degree 2190 [*Claessens and Hirt,* 2013] and with even higher resolution for the topographic gravity component to degree 10,800 in the context of UNESCO's World Gravity Map [*Bonvalot et al.,* 2012; *Balmino et al.*, 2012]. For the Moon and the other terrestrial planets, Bouguer gravity maps were produced, too, see *Watters et al.* [2007] and *Zuber et al.* [2012].

Opposed to planetary sciences [e.g., *Wieczorek and Phillips,* 1998], the construction of global Bouguer gravity maps based on spectral techniques is relatively new to Earth sciences. As such, it is important to carefully check and verify the modelling techniques involved for the Earth sciences user community to gain confidence in the new global Bouguer maps and to provide an advanced validation scheme for any planetary Bouguer gravity map. The necessity for validation of the spectral method has been recently acknowledged in the literature, e.g., *Gruber et al.* [2014].

However, only few studies are actually concerned with the validation of topographic gravity from spectral-domain modelling with high resolution (degree-2160, equivalent to ~10 km resolution, or even finer): *Wang et al.* [2010] compared topographic gravity, as obtained from evaluation of Newton's integral (1) in the spatial domain and (2) from spherical harmonic expansions of the topographic potential to degree 2700. They encountered notable discrepancies at the 10-30 mGal level over steep mountain slopes of Earth's major mountain ranges, with a maximum disagreement at the ~60 mGal level in the Himalayas. *Balmino et al.* [2012] compared topographic gravity from the spatial and spectral method to ultra-high degree of 10,800 (~1 km resolution), yielding maximum differences of ~40 mGal and a root-mean-square (RMS) of ~2.3 mGal over parts of Northern Africa, which, however, increases in the Atlas mountain range to the ~10 mGal level.

With the EGM2008 model expanded to its full ~10 km spatial resolution, gravity anomalies are known to an accuracy of ~1 to ~3 mGal over wide parts of the Earth's surface [cf. *Pavlis et al.* 2008, p.8]. For reliable interpretation of Bouguer gravity anomalies from EGM2008 (or other GGMs of similar precision), it is thus reasonable to require an uncertainty well below the 1 mGal-level for the topographic gravity component that the Bouguer map relies on. Then, errors associated with the topographic gravity computation become negligible. However, the aforementioned validation results do not provide evidence for adequate accuracy of the topographic gravity component in global Bouguer gravity maps.

As goal of the present study, we present an advanced validation based on *Hirt and Kuhn* [2014] for the computation of Earth's topographic gravity field with spectral techniques. As spherical harmonic model of the global topography, Curtin University's Earth2012 product is used to degree-2160, which is commensurate with the EGM2008 resolution (Sect. 2). Our validation strategy relies on comparisons between spatial-domain (Sect. 3.1) and spectral-domain (Sect. 3.2) gravity

forward modelling providing a comprehensive cross-check on the gravity computation procedures (Sect. 4).

To facilitate the validation, we develop a largely complete spherical harmonic expansion of the topographic gravity field, as implied by a degree-2160 global topography. This involves expansion of the topographic potential to 15th integer power of the topography and modelling to ultra-high harmonic degree of ~21,600 being the 10th multiple of the input band-width. By way of background, degree-2160 modelling in past work never exceeded the 10th integer power and frequencies beyond the input band-width were not considered at all. As such, the gravity field of a degree-2160 (10 km resolution) topography is computed and its spectrum characterized with great completeness for the first time to unprecedented fine spatial scales of ~1 km in spherical harmonics (Sect. 5.1). Numerical comparisons between gravity from our new spherical harmonic expansion of the topographic potential to degree 21,600 against gravity from high-resolution Newtonian integration are presented and discussed in Sect. 5.2 and 5.3 for local and global test areas. Our comparisons are relevant for modern Bouguer gravity maps from EGM2008 and other such models (which incorporate newer or improved data, for instance based on the GOCE satellite mission) in general, and for spectral-domain gravity forward modelling to high resolution in particular (Sect. 6 and 7).

2. Data

As model describing the global topographic masses, the spherical harmonic expansion of Curtin University's rock-equivalent topography (RET) model RET2012 [e.g. *Hirt,* 2013] is used in this study, which is freely available via http://geodesy.curtin.edu.au/research/models/Earth2012/, file Earth2012.RET2012.SHCto2160.dat). RET2012 represents Earth's RET topography to harmonic degree and order 2160, which corresponds to 5 arc-min spatial resolution (half wavelength). Over land areas, the RET2012 model relies on data from (1) the Shuttle Radar Topography Mission (SRTM) version 4.1, cf. *Jarvis et al.* [2008], (2) SRTM30_PLUS (version 7) bathymetry [*Becker et al.,* 2009] over the oceans and some of Earth's major lakes, and (3) ETOPO1-derived ice sheet heights [*Amante and Eakins* 2009] over parts of Antarctica and Greenland. We acknowledge that newer topography models such as Earth2014 [*Hirt and Rexer,* 2015] have recently become available, relying on more up-to-date data sets over the oceans and ice-shields. However, to investigate the spectral characteristics of a degree-2160 topographic gravity field, and to validate the computational techniques for spectral forward modelling at 5 arc-min resolution, the chosen RET2012 topography model is considered as sufficient (also see below).

3. Methods

The spherical harmonic expansion of the RET2012 model is used as input topography mass model both in spatial-domain forward modelling (Newtonian integration) cf. Sect. 3.1 and in spectral forward modelling (Sect. 3.2). RET heights rely on the concept of equivalence between a given mass distribution represented by height and density and the mass distribution described by RET height and one constant reference density [*Rummel et al.,* 1988; *Kuhn and Seitz,* 2005; *Kuhn and*

Hirt, 2016]. The RET2012 model used here describes all topographic masses (ice, water, rock) with a single constant density value ρ_{Rock} of topographic rock (2670 kg m^{-3}). This was accomplished by compressing ice masses (ρ_{Ice} = 917 kg m^{-3}) and water masses (ρ_{Ocean} = 1023 kg m^{-3}, ρ_{Lake} = 1000 kg m^{-3}) into layers of equivalent topographic rock following the concept of *Rummel et al.* [1988]:

$$H_{RET} = H_{BED} + \frac{\rho}{\rho_{Rock}} \Delta H \tag{1}$$

with H_{RET} the RET height, ρ_{Rock} the mass-density of topographic rock and ρ the mass-density of the mass anomaly (e.g. ice or water), H_{BED} bedrock height (lower bound) of the mass body and ΔH the thickness of the mass body.

As advantage of the RET concept, it is possible to calculate implied gravity effects over land, ocean and ice sheets based on one single mass density, without the need to distinguish between different density values in forward modelling [*Hirt and Kuhn,* 2012]. Thus, some complexity associated with modelling the short-scale gravity fields of individual mass bodies (lakes, oceans, ice shields) is avoided and a clearer focus on the study and validation of the short-scale gravity field of the topographic masses is achieved. While a disadvantage of the RET compression relates to approximation errors because the geometry of mass anomalies (Eq. 1) is changed [*Kuhn and Hirt,* 2016] it is not considered a problem in this study when comparing gravity forward modelling techniques based on identical mass distributions.

Ultra-short scale modelling of the ocean and ice masses through a mass-layer approach [e.g., *Tenzer et al.,* 2010; *Rexer et al.* 2016] and the topographic potential in ellipsoidal instead of spherical approximation [e.g., *Claessens and Hirt,* 2013; *Rexer et al.,* 2016] goes beyond the scope of the present paper. As an important benefit of choosing spherical approximation level over ellipsoidal approximation for this paper, the characteristics of the short-scale gravity field constituents can be studied for various harmonic bands, which is not possible when the modelling is based on ellipsoidal approximation (cf. *Claessens and Hirt* [2013]).

Both in spatial and spectral forward modelling, the full expansion of the RET2012 topography model is used (i.e., harmonic degrees 0 to 2160), along with the same modelling parameters (reference radius R = 6378137 m, mass-density ρ_{Rock} = 2670 kg m^{-3} and gravitational constant G = $6.67384 \cdot 10^{-11}$ m^3 kg^{-1} s^{-2}). This is to ensure that the same mass model is consistently used in both forward modelling techniques. In both methods, RET2012 heights H are synthesized using

$$H(\varphi, \lambda) = \sum_{n=0}^{2,160} \sum_{m=0}^{n} \left(\overline{HC}_{nm} \cos(m\lambda) + \overline{HS}_{nm} \sin(m\lambda) \right) \bar{P}_{nm}(\sin \varphi) \tag{2}$$

with φ, λ denoting the geocentric coordinates of the computation point, $(\overline{HC}_{nm}, \overline{HS}_{nm})$ the fully-normalized spherical harmonic coefficients of degree n and order m, and $\bar{P}_{nm}(\sin \varphi)$ the fully-normalized Associated Legendre Functions (ALFs). The methods applied are outlined in Sect. 3.1 and 3.2 in a more general sense, while computational details are given in Sects. 4.1 and 4.2.

3.1   Spatial domain forward modelling

Our spatial domain forward modelling uses *discretised* Newtonian integration [e.g., *Kuhn,* 2000; Kuhn 2003; *Kuhn et al.,* 2009], which follows exactly the same approach as employed in *Hirt and Kuhn* [2014]. In this approach the gravitational signal of a given mass distribution (e.g. topographic masses) is obtained by the gravitational effects generated through a series of regular shaped mass elements (e.g. point mass, rectangular prism or tesseroid) that discretize the mass distribution considered. We discretize the global topographic masses (incl. bathymetry) by a series of spherical volume elements (e.g. tesseroids in spherical approximation) limited by surfaces of constant geographic longitude, latitude and spherical radius (cf. Figure 1 in *Hirt and Kuhn* [2014]). The tesseroids are further approximated by rectangular prisms with identical vertical extension. The spatial extension of each prism is selected such that first-order mass equivalence is obtained according to e.g. *Anderson* [1976], *Grüninger* [1990], *Heck and Seitz* [2007]. The advantage of this approach is the possibility to employ closed analytical formulae for the gravitational effect of a rectangular prism. We use the well-known analytical formulae provided by, e.g., *Mader* [1951], and *Nagy et al.* [2000] modified to a numerically more stable expression (cf. *Kuhn* [2000] and *Heck and Seitz* [2007]).
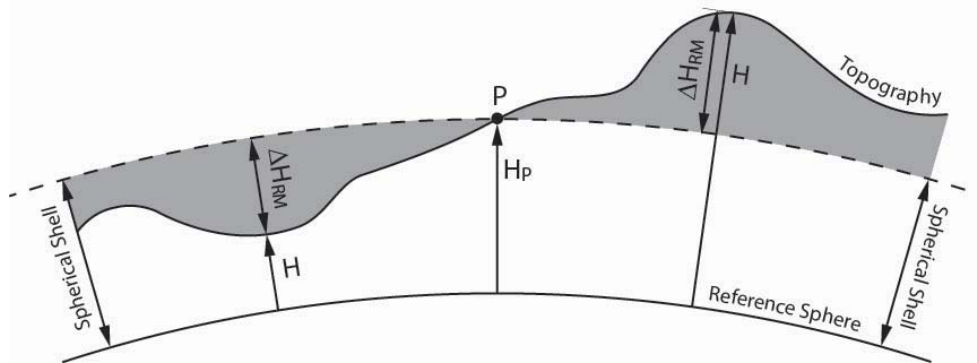

Figure 1. Principle of the spherical terrain correction for topographic masses. At the computation point P the gravitational attraction of the topographic masses δg is derived through the gravitational attraction δg^{SH} of the spherical shell with thickness H_P and the spherical terrain correction obtained through the gravitational attraction δg^{RM} of all masses residual to the spherical shell and characterized by the height difference ΔH_{RM}.

The approximation error introduced through *discretised* Newtonian integration depends on how well the discretised mass distribution approximates the given mass distribution, which in turn depends on the shape and size (resolution) of the mass elements selected. As pointed out in *Hirt and Kuhn* [2014], the use of rectangular prisms is approximate, when using spherical approximation, as adjoining prisms intersect towards the bottom and exhibit wedge-like gaps towards the top. However, the approximation error can be largely reduced through the selection of small (both spatial and vertical extension) prisms in the near vicinity of the computation point. Similar to results obtained in *Hirt and Kuhn* [2014], this study demonstrates that the approximation error can be reduced to levels on the order of 2 μGal (RMS) as obtained by numerical comparison between space and spectral domain techniques (see section 4). Further we use the concept of

spherical terrain corrections (e.g. *Kuhn et al.* [2009]) to limit the vertical extension of prisms in the vicinity of the computation point. Hereby the gravitational attraction of the global topographic masses is derived according to

$$\delta g = \delta g^{SH} + \delta g^{RM} \tag{3}$$

where δg^{SH} is the gravitational attraction of a spherical shell (often termed Bouguer shell) and δg^{RM} is the gravitational attraction of all masses residual to the shell (e.g. spherical terrain correction; cf Figure 1). In this approach the vertical extension of the shell is selected so that no residual masses are present at the location of the computation point. Only δg^{RM} is derived through discretised Newtonian integration while δg^{SH} is obtained through the analytical formula for the Bouguer shell (e.g. *Vaniček et al.* [2001]).

3.2 Spectral domain forward modelling

The topographic potential, as generated by the topographic mass model, is computed in the spectral domain with the forward modelling technique described in *Hirt and Kuhn* [2014]. Given the relation between topography and gravity is non-linear, the topographic potential is expressed as a series expansion of integer powers p of the topography [e.g., *Rummel et al.* 1988; *Wieczorek* 2007; 2015]. Although our topographic mass model is strictly band-limited (to spectral band of degrees 0 to 2,160), it generates – in good approximation – a full-spectrum gravity field [*Balmino* 1994; *Hirt and Kuhn,* 2014] with spectral energy at spatial scales far beyond degree 2,160. Following *Hirt and Kuhn* [2014], any integer power p of a band-limited topography expanded to degree n delivers spectral constituents of the topographic potential up to degree $p \cdot n$. In our work, contributions of integer powers of $p \in [1\ 15]$ to the topographic potential are taken into account up to a spherical harmonic degree of $n_{max} = 21,600$.

The spectral method requires expansion of heights H from the topography model onto a global grid [Eq. (2)]. Topographic height functions (THF) are formed as H/R and raised to integer power p in the space domain, giving $H^{(p)} = (H/R)^{(p)}$. Harmonic analysis delivers the spherical harmonic coefficients $H_{nm}^{(p)} = \overline{HC}_{nm}^{(p)}, \overline{HS}_{nm}^{(p)}$ of the integer powers of the THFs. The sets of $H_{nm}^{(p)}$–coefficients are used to calculate the coefficients of the topographic potential V_{nm} following *(Chao and Rubincam* [1989], *Balmino* [1994], *Balmino et al.* [2012], *Wieczorek* [2007, 2015])*

$$V_{nm} = \frac{1}{2n+1} \frac{4\pi R^3 \rho}{M} \sum_{p=1}^{p_{max}} \frac{\prod_{i=1}^{p}(n+4-i)}{p!\,(n+3)} H_{nm}^{(p)} \tag{4}$$

with V_{nm} as short-hand for $(\overline{VC}_{nm}\ \overline{VS}_{nm})$, $M = 5.9725810 \cdot 10^{24}$ kg as Earth's mass including the atmosphere, and p_{max} as maximum integer power of the series expansion. Next, the V_{nm} are used to compute gravity disturbances δg (radial derivatives of the topographic potential) at the topographic surface, here represented by the RET2012 heights. This task is accomplished using the gradient approach for 3D spherical harmonic synthesis [*Hirt and Kuhn,* 2012]. In brief, the gradient

approach is a numerically efficient approximation technique to compute dense grids of gravity disturbances at irregular surfaces [*Hirt*, 2012]. Grids of gravity disturbances and their higher-order radial derivatives are computed at some constant height H_{ref} above the reference sphere of radius R and continued to the computation point P(φ, λ, H) residing at the topography (H) using

$$\delta g \ (\varphi, \lambda, H) \approx \sum_{k=0}^{k_{max}} \frac{1}{k!} \frac{\partial^k \delta g}{\partial r^k} \Big|_{r=R+H_{ref}} \left(H - H_{ref}\right)^k \tag{5}$$

where k denotes the order of radial derivative $\partial^k \delta g / \partial r^k$ of the gravity disturbance , k_{max} the maximum order of the Taylor series expansion, and $r = R + H_{ref}$ a constant radius of evaluation. See *Hirt and Kuhn* [2012] for the equation of the k-th order radial derivative of δg. Field continuation with gradients has also been applied in *Balmino et al.* [2012], however, without using mean constant heights H_{ref} which were shown in *Hirt* [2012] to accelerate the convergence of the continuation.

4. Computations

Both forward modelling techniques were applied (i) locally over a test area in the Himalaya Mountains with 1 arc-min spatial resolution of the computation points and (ii) globally at reduced resolution of 5 arc-min. The first experiment, designed similar to that presented in *Hirt and Kuhn* [2014] but with increased spectral resolution provides a detailed local view on the agreement between the two methods, while the second experiment provides insight on a truly global scale, and therefore facilitates the validation of topographic gravity modelling around the globe.

4.1 Newton integration

For the discretized Newtonian integration approach (Sect. 3.1), topographic heights from the RET2012 topography have been synthesized (Eq. 2) with extremely high spatial resolution in the vicinity (near-zone) of the computation points (Table 1). For the local experiment, the topography is sampled at 5 arc-sec resolution (up to 0.5 degree distance around any computation point). With an oversampling of factor 60 (5 arc-sec sampling vs. 5 arc-min nominal resolution associated with a degree 2,160 expansion), the spherical harmonic topography is very well represented in the space domain. The topography was oversampled in order to minimize numerical integration errors associated with the discretisation of the topographic mass model (cf. Section 5). For the global experiment, the global topography is represented at 30 arc-sec resolution up to 3 degrees around the computation point, resulting in a lower oversampling factor of 10. Note that while the topography has been sampled with high spatial resolution (Table 1), the computation points are arranged on a 1 arc-min resolution grid (local experiment, 14,400 computation points) and 5 arc-min (global experiment, ~9.33 million points).

In order to accelerate the computation without compromising the accuracy, a number of coarser grid resolutions were used for source masses located more distant from a computation point. The use of such grid cascades is common practice (e.g., *Forsberg* [1984]) and permitted due to the

quadratic attenuation of gravitational attraction with distance. The coarser resolutions and spatial extensions around a computation point were selected empirically so that the corresponding approximation error with respect to the next finer resolution always remained below 1 μGal. Coarser resolutions have been derived by arithmetically averaging finer resolutions to ensure mass equivalence between resolutions. Table 1 details the spatial resolutions and extensions for the local experiment (6 grid cascades) and the global experiment (4 grid cascades), from highest resolution (near-zone) to lowest resolution (far-zone) for the remote topographic masses.

Table. 1. Details on Newtonian integration as applied in the local and global experiments: Spatial resolution, area of computation points, grid resolutions (data points), oversampling factors and overall computation times for both experiments. Spatial extensions for each grid are given as arc-distances along parallels and meridians. Spatial resolutions of the grid cascades are selected so to seamlessly join, e.g. a coarser resolution is obtained as an integer multiple of the finer resolution.

	Local experiment	Global experiment
Input model	RET2012 topography in band 0 to 2,160	
Computation point resolution	1 arc-min	5 arc-min
Computation area	2 deg x 2 deg	180 deg x 360 deg
Number of computation points	120 x 120	2160 x 4320
Data points (grid cascades)	5 arc-sec (to 0.5 deg)	30 arc-sec (to 3 deg)
	10 arc-sec (to 1 deg)	1 arc-min (to 6 deg)
	20 arc-sec (to 3 deg)	3 arc-min (to 20 deg)
	1 arc-min (to 10 deg)	15 arc-min (far zone)
	3 arc-min (to 30 deg)	
	9 arc-min (far zone)	
Oversampling factor (near-zone)	60	10
CPU-hours	35	10,000

Due to the very high computational burden for the global experiment, the space domain forward modelling has been performed on Western Australia's supercomputer *Magnus* operated by the Pawsey Supercomputing Center. Magnus is a Cray XC40 system hosting Xeon E5-2690V3 "Haswell" processors running at 2.6 GHz, for a total of 35,712 cores, delivering in excess of 1 PetaFLOP of computing power (see https://www.pawsey.org.au/). For parallel computations the 5 arc minute resolution computation point grid over the test area has been divided into 10° × 10° tiles each containing 14,400 computation points. While the global calculation of gravity disturbances at 5 arc-min resolution required a total of ~10,000 CPU hours, the parallel processing of all tiles allowed the computation to be completed within less than 2 days.

4.2 Spectral modelling

For the spectral forward modelling, heights H were synthesized from the RET2012 topographic mass model in spectral band of degrees [0 2,160]. THFs were formed for each integer power $p \in$ [1 15], and their SHCs $H_{nm}^{(p)}$ derived through spherical harmonic analysis. For the harmonic

analysis, we use *Gauß-Legendre-Quadrature* implemented in the SHTools package (http://shtools.ipgp.fr/). The SHTools were modified 1) with the *Fukushima* [2012] routines for stable computation of ALFs to ultra-high degree (beyond degree ~2,700) and 2) with OpenMP parallel directives for achieving moderate computation times, as described in detail in *Rexer and Hirt* [2015]. The contribution of the $H_{nm}^{(p)}$ to the topographic potential $V_{nm}^{(p)}$ and (total) topographic potential $V_{nm} = \sum_{p=1}^{15} V_{nm}^{(p)}$ were computed with Eq. 4. Each set of $H_{nm}^{(p)}$ and $V_{nm}^{(p)}$ SHCs is complete to $n_{max} = 21,600$ and comprises ~233.3 million pairs of harmonic coefficients.

In our study contributions up to the 15th power of the topography ($p_{max} = 15$) are taken into account. The necessary grid resolution Δx for each spherical harmonic analysis can be determined by the integer power p, in order recover the spectral constituents of each THF without aliasing:

$$\Delta x(p) = p^{-1} \cdot 5 \text{ arc-min} \tag{6}$$

For $p = 1$, the necessary grid resolution Δx is 5 arc-min (2,161 x 4,321 grid points), for $p = 2$, $\Delta x = 2.5$ arc-min (4,321 x 8641 points) and for $p = 15$, $\Delta x = 20$ arc-sec (32,401 x 64,801 grid points). We fully recovered the SHCs of the THFs up to $n_{max} = 21,600$, For $p > 10$, the THFs contain spectral energy beyond $n_{max} = 21,600$. However, coefficients of degree $> 21,600$ were not further taken into account here. From our numerical study, evidence is obtained that the signal power associated with $n > 21,600$ is safely negligible (Sect. 5).

Gravity disturbances dg were obtained from the $V_{nm}^{(p)}$ and V_{nm}- SHCs through 3D-synthesis (Eq. [5]) at exactly the same computation points P(φ, λ, H) used in the Newtonian integration, with the heights H taken from the RET2012 topography model. Importantly, computation point heights H are set to zero when $H < 0$, thus reside at the surface of the reference sphere (e.g., over the oceans). This is to avoid gravity syntheses inside the reference sphere. For the 3D-syntheses, the isGrafLab software by *Bucha and Janák* [2014] was used that incorporates the gradient continuation approach [*Hirt,* 2012] and the *Fukushima* [2012] routines for stable gravity synthesis to ultra-high degree. As an alternative to the *Fukushima* [2012] methods, the approach by *Jekeli* et al. [2007] *and Balmino et al.* [2012] could be used whereby insignificant terms in the synthesis are not evaluated in order to increase the computational efficiency.

Prior to the 3D-synthesis, convergence tests were carried out in order to determine the required order of Taylor expansions k_{max} in the 3D-synthesis. By comparing approximate dg-values from various Taylor orders $k_{max} \in [1\ 20]$ with exact values computed at selected 3D-locations *without* gradients at P(φ, λ, H), the convergence of Eq. (5) was investigated [also see *Hirt and Kuhn,* 2012; *Balmino et al.,* 2012; *Bucha and Janák,* 2014]. For the reference height H_{ref} a value of 3000 m was used, keeping the distances $H - H_{ref}$ always smaller than 4000 m, considering the range of topographic heights from 0 to ~6680 m. As a result, the number of terms required for convergence of the Taylor series (Eq. 5) is much reduced (in comparison to using $r = R$ as radius of evaluation). For our test points (located at $H = 0$ above deep ocean trenches and at H = 6679.143 m over the Himalayas), convergence (i.e. differences between approximate and exact δg-values fall below the

0.1 microGal threshold) was reached for $k_{max} = 15$, the value of which is used in all syntheses in our study. Note that this value is about twice as large as for a topographic potential truncated to degree 2,160 [cf. *Hirt and Kuhn*, 2012], reflecting the influence of the short-scale gravity signals (in band [2,161 to 21,600]) on the gravity continuation with Eq. (5).

Overall, for the spherical harmonic analyses, conversion of $H_{nm}^{(p)}$ to $V_{nm}^{(p)}$ and subsequent spherical harmonic syntheses, an estimated ~5,000 CPU hours were required, which is about half of the CPU time used for the numerical integration (Sect. 4.1).

5. Results

5.1 Degree variances

The dimensionless degree variances of the THFs

$$\sigma_{H_n^{(p)}}^2 = \sum_{m=0}^{n} \left(\overline{HC}_{nm}^{(p)2} + \overline{HS}_{nm}^{(p)2} \right) \tag{7}$$

and of the (single) contributions to the topographic potential model

$$\sigma_{V_n^{(p)}}^2 = \sum_{m=0}^{n} \left(\overline{VC}_{nm}^{(p)2} + \overline{VS}_{nm}^{(p)2} \right) \tag{8}$$

are shown in Fig. 2 and 3 as a function of the harmonic degree n. Both figures clearly show that raising the band-limited (to degree $n = 2,160$) THF (H/R) to integer power p produces spectral energy to harmonic degree $p \cdot n$ [cf. *Hirt and Kuhn,* 2014, Fig 2. ibid]. While there is a pronounced drop in spectral energy near degree $p \cdot n$ for the low integer powers (say up to 5), the higher integer powers of the THF exhibit a rather smooth, continuous decay in energy over all of their spectrum that reaches the noise level at degree $p \cdot n$ (Fig. 2).

Fig. 3 shows the contribution made by each of the THFs to the topographic potential (various colors) as well as the spectrum of the topographic potential as the sum of all contributions (black line). The spectrum of the topographic potential experiences a sharp drop of ~2 orders of magnitude (from 10^{-20} to 10^{-22}) at degree $n = 2,160$, showing that the bulk of spectral energy of the potential is concentrated in the band-width [0 2,160] of the input topography. The multiples of the input band-width are dominated by the higher-order integer powers, e.g., the second multiple, band [2,161 4,320] by $p \in [2\ 5]$ and the third multiple (band [4,321 6,420]) by the contributions associated with $p \in [3\ 11]$. In the fourth and fifth multiple (i.e., to $= 10,800$), all higher order-powers to $p \approx 15$ make quite comparable contributions to the topographic potential. For $n > 17,280$ the spectrum is dominantly defined through the highest integer powers ($p = 15$) considered here, suggesting that spectral modelling is not entirely complete in the highest degrees. Notwithstanding, global comparisons (Sect 4.3) will demonstrate that the level of completeness achieved here is good enough for accurate spectral gravity forward modelling.

Fig. 3 shows that the spectral energy of the topographic potential experiences quite a slow decay beyond degree $n = 2,160$, from the level of 10^{-22} to 10^{-25} ($n = 10,800$). The spectral energy of

the potential generated by our degree 2,160-topography falls below the 10^{-25}-level around degree $n = \sim 10,800$. In summary Fig. 3 demonstrates the importance of the higher-order integer powers for modelling of the topographic gravitational signals at short spatial scales, beyond the resolution of the input topography mass model.
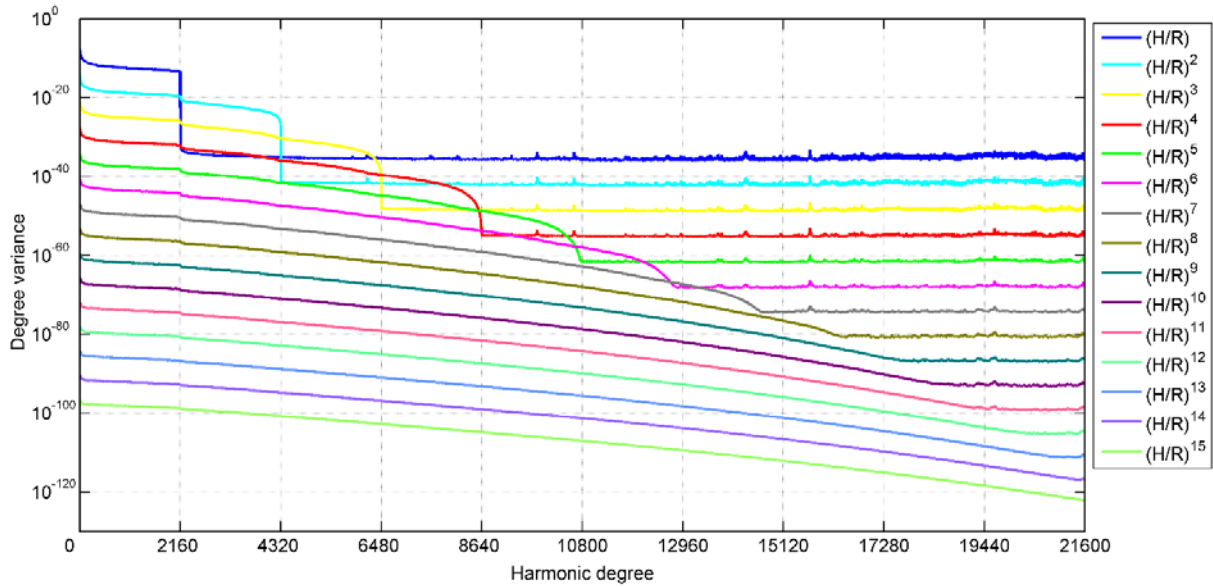

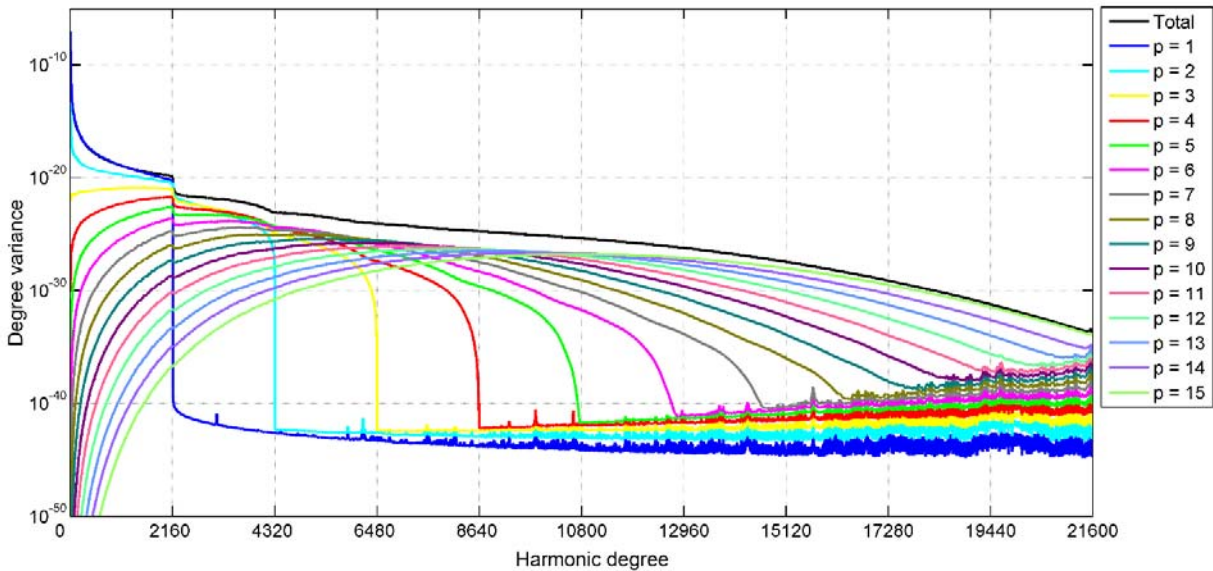**Figure 2.** Degree variances of the first fifteen integer powers p of the topographic height function (H/R) from the model RET2012 up to degree 2160.

Figure 3. Degree variances of the first fifteen powers of the topographic potential from the model RET2012 up to degree 21,600 and total contribution (black line).

5.2 Local experiment

As the test area for the local experiment, a 2 x 2 degrees area in the Himalayas (27° to 29° geocentric latitude and 84° to 86° longitude) was selected. With a range in elevation of ~6700 m (in the degree-2160 RET2012 model), this area features rough topography, including the Mount Everest Summit as well as low-lying terrain (Fig. 4a). Fig. 4b shows gravity disturbances from spectral forward-modelling (computed here to $n_{max} = 21,600$ and $p_{max} = 15$ with Eqs. [4] and [5]) over the test area. From Fig. 4c, these are in excellent agreement with those from Newtonian integration (computed at 1 arc-min resolution from highest-resolution elevation grids, cf. Table 1, "local experiment" for details). The maximum value of the differences between the results of the two different approaches is ~15 µGal and the root-mean-square (RMS) is ~2 µGal (Fig. 4c).
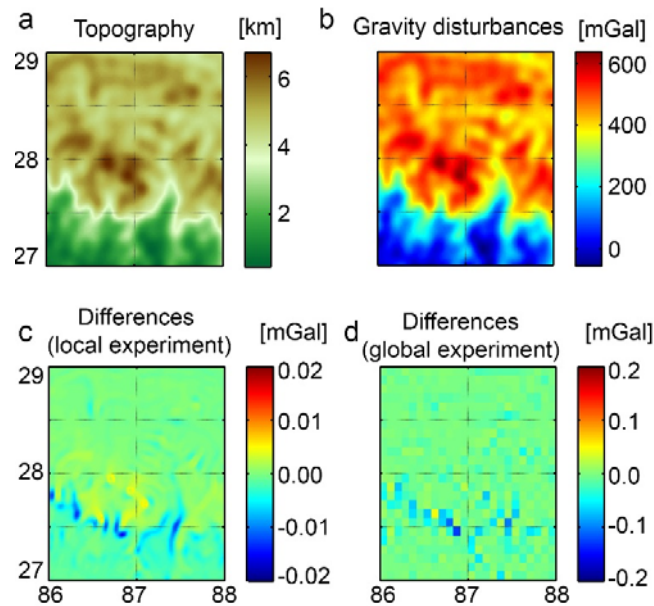

Figure 4. Results of the local and global experiment over Himalaya test area: (a) topography at 1 arc-min resolution; (b) gravity disturbances from the spectral method (N_{max} = 21,600) at 1 arc-min resolution (c) differences between gravity disturbances from spectral modelling and Newtonian integration (use of high-resolution integration, cf. Table 1) at 1 arc-min resolution, (d) as before, but Newtonian integration at 5 arc-min resolution and lower oversampling factor (global experiment). The comparison between panels (c) and (d) exemplifies the increased level of discretisation errors in the global experiment. Note the different color scales in panels (c) and (d). Unit in km (a) and mGal (b-d).

For the spectral approach over the Himalaya test area, Fig. 5a gives a detailed breakdown of RMS signal strengths of gravity disturbances at the Earth's surface for the single contributions $p \in$ [1 15] (vertical axis) and spectral windows, from band [0 2,160] to [19440 21,600] (horizontal axis). As expected, the largest contribution is made by the linear term ($p = 1$, RMS = ~394 mGal). Integer powers $p = 2$ to 5 contribute ~20, ~6, ~2 and ~1 mGal signals in band [0 2,160]. Significant signals at the ~1mGal level are generated by the second multiple (band [2,161 4320], $p \in$ [2 4]), while the signal strengths associated with $p < 7$ and $n < 6420$ reach 0.1 mGal or more (yellow). RMS-contributions at the 10-µGal level (green) and 1-µGal level (light

blue) are made by various multiples and integer powers, up to $n = {\sim}12{,}960$ and $p = 15$. Fig 5a also shows which spectral contributions are non-existent (white) or insignificant (dark blue) over our test area.
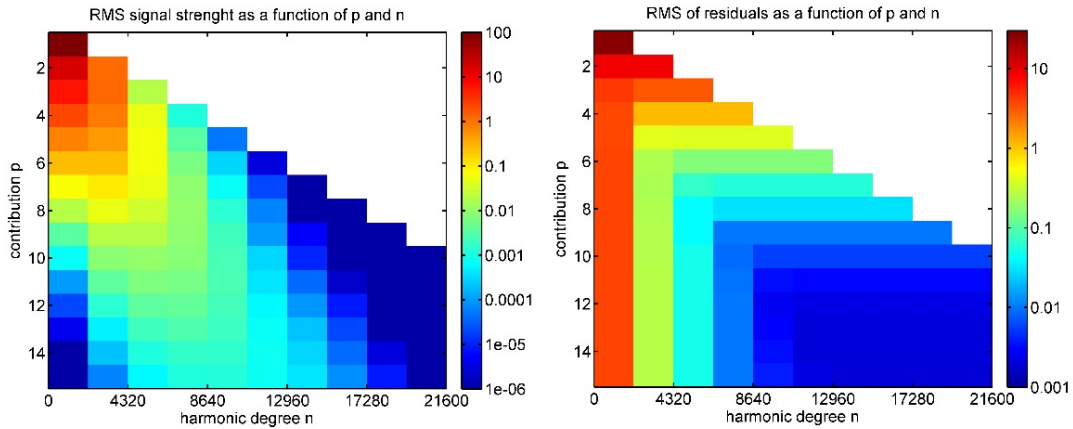

Figure 5. Local experiment: (a) RMS (root-mean-square) signal strengths of gravity disturbances from the RET2012 topography model evaluated at the Earth's surface as a function of the contribution *p* (vertical axis) and spectral bands (multiples of 2,160 harmonic degrees *n,* horizontal axis) over the Himalaya test area, unit in mGal. (b) RMS of residuals (= differences between gravity disturbances from spectral modelling minus Newtonian integration) as a function of maximum contribution p_{max} taken into account and harmonic degree *n.* Unit in mGal, number of computation points is 14,400.

Fig. 5b provides a detailed look at the agreement between gravity disturbances from Newtonian integration and spectral modelling, as a function of the maximum harmonic degree n_{max} and maximum integer power p_{max} used in Eq. (4). The RMS-values generally decrease the higher n_{max} and p_{max}, with the ~1 mGal level reached for $p_{max} = 4$ and $n_{max} = 4320$ and the best agreement (~2 μGal RMS level) reached for $p_{max} = 13$ and $n_{max} = 12{,}960$. For higher powers and harmonic degrees considered in the modelling, the agreement remains at the ~2 μGal level (cf. Fig. 4b and 5b) over our local test area, suggesting that the residuals between both methods mostly reflect numerical integration errors. Importantly, Fig. 5b shows that the RMS of the gravity disturbance differences (between both methods) would stay at the 4 mGal-level (22 mGal maximum differences) if the gravity signals were modelled to $n_{max} = 2{,}160$ only. This emphasizes the importance of short-scale spectral modelling to ensure consistency with the Newtonian integration.

5.3 Global experiment

The global experiment provides insight into the agreement of gravity disturbances from both methods across the globe. Because of the large number of computation points (~9.3 million at 5 arc-min resolution vs. 14,400 in the local experiment), the resolution of the near-zone topography in the numerical integration had to be lowered from 5 arc-sec to 30 arc-sec (Table 1). As a consequence, the oversampling of the degree-2160 topography is reduced from factor 60 down to 10. Fig. 6 shows the global grid of gravity disturbances from Newtonian integration and Table 2

reports the descriptive statistics of gravity disturbances from both methods, of the differences "spectral modelling minus Newtonian integration" and of the signal strengths associated with the input-band width [0 2,160] and additional nine multiples. Fig. 7 shows the global differences between gravity disturbances from spectral forward modelling ($p_{max} = 15$, $n_{max} = 21,600$, $k_{max} = 15$) and Newtonian integration. From Table 2 and Fig. 7, the global statistics of both solutions are in very good agreement, with the differences being at the ~8 μGal level (RMS).
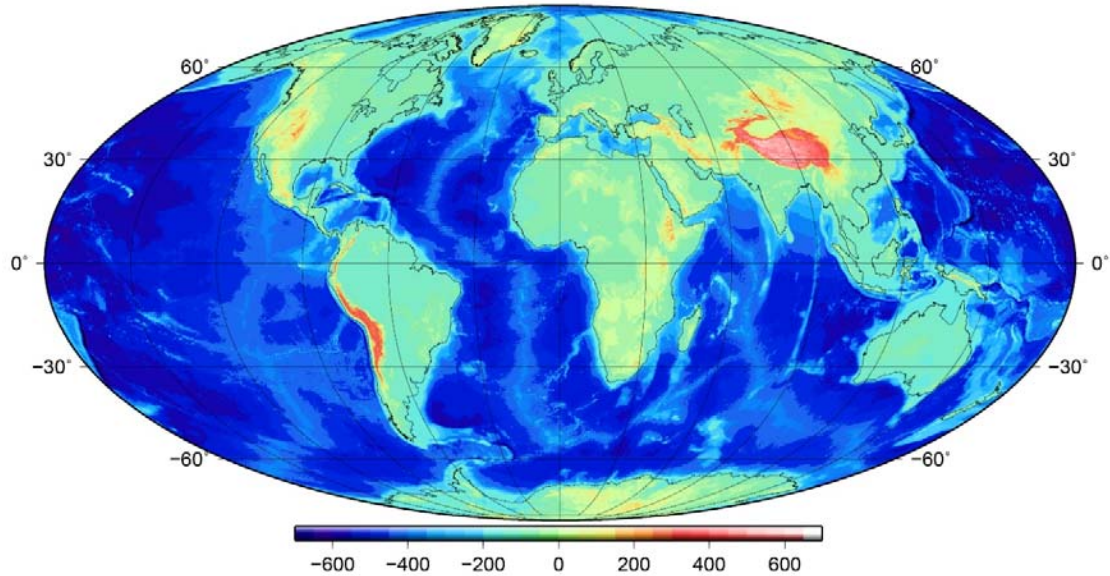

Figure 6. Global experiment: Gravity disturbances at the Earth's surface from Newtonian integration at 5 arc-min resolution. Unit in mGal, Mollweide projection.
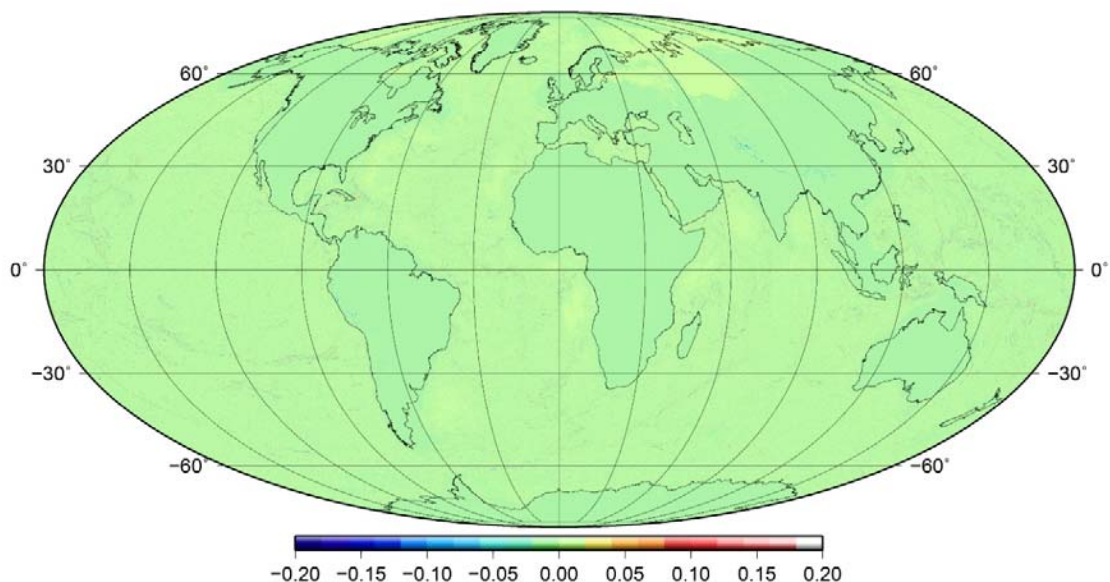

Figure 7: Global experiment: Differences between gravity disturbances from spectral modelling ($N_{max} = 21,600$) and Newtonian integration at 5 arc-min resolution at Earth's surface. Unit in mGal, Mollweide projection.

Table 2. Descriptive statistics of gravity disturbances in various spectral bands. Gravity disturbances were evaluated at the RET2012 topographic surface (and at H=0 m over the oceans) at 5 arc-min resolution globally. Units in mGal.

Result or spectral band	Min	Max	Mean	RMS
Spectral (0 to 21600)	-837.5964	627.0566	-281.5447	348.5240
Newtonian integration	-837.5661	627.0558	-281.5461	348.5233
Spectral minus integration [a]	-1.2603	0.5211	-0.006	0.0083
0 to 2160	-837.8613	627.3182	-281.5451	348.5248
2161 to 4320	-30.5665	43.8098	0.0003	0.5137
4321 to 6480	-12.9055	7.1085	0.0001	0.0405
6481 to 8640	-8.5055	4.7439	0.0000	0.0144
8641 to 10800	-3.2267	5.6946	0.0000	0.0083
10801 to 12960	-2.3412	2.3242	-0.0000	0.0048
12961 to 15120	-1.6076	0.7966	-0.0000	0.0020
15121 to 17280	-0.2114	0.2774	0.0000	0.0005
17281 to 19440	-0.0368	0.0412	0.0000	0.0001
19441 to 21600	-0.0036	0.0032	0.0000	0.0000

[a] cells closer than 1° to the poles excluded.

Over land areas, gravity disturbances from both approaches are in 3.6 μGal RMS agreement (maximum difference 0.36 mGal), while the discrepancies are about three times higher over the oceans with 10 μGal RMS (maximum difference ~1.26 mGal), cf. Table 3 and Fig. 7. In comparison between land and ocean areas, overall land topography is smoother than bathymetry, which is reflected through increased discrepancies between both methods, particularly along ocean trenches and sea-floor ridges (Fig. 7).

In comparison to the extremely detailed numerical integration applied in our local experiment (Table 1), the RMS agreement over the 2 x 2 degrees Himalaya area deteriorates in our global computation from 2 μGal to 18μGal and maximum discrepancies increase from 0.02 mGal to 0.12 mGal (compare Fig. 4c and 4d). The only parameter changed between the global and local experiments is the resolution of topography grids (Table 1), and thus the oversampling factor of the near-zone topography (factor 60 vs. 10). Hence, it is the discretisation error in the numerical integration associated with the reduced oversampling that is primarily reflected by the differences in Fig. 7.

Table 2 (bottom part) reports the signal strengths of gravity disturbances in ten spectral bands of 2,160 degrees width, from [0 2160] up to [19,440 21,600]. While the RMS as a measure for the average signal strength quickly drops, from ~0.5 mGal ([2,161 4,320]) below the ~1 μGal level (beyond degrees 15,120), there are gravity signal contributions with mGal-amplitudes present up to ultra-high degrees (say, 15,120). A comparison between Newtonian integration and spectral forward modelling with varying maximum harmonic degree $n_{max} \in [2,160 \ 4,320 ... 21,600]$ shows that modelling of these very short-scale gravity signals improves the (global) agreement with Newtonian integration up to degree ~17,280 (cf. Table 3).

Table 3. Statistics of gravity differences "spectral modelling minus Newtonian integration" over land areas (# 3,130,130 cells) and ocean areas (# 6,114,670 cells), reported as a function of the maximum harmonic degree of the spectral model. Cells closer than 1° to the poles excluded. Unit in mGal.

Spectral band	Land cells		Ocean cells	
	Abs(max,min)	RMS	Abs(max,min)	RMS
0 to 2160	38.7	0.721	29.6	0.359
0 to 4320	8.7	0.061	2.7	0.022
0 to 6480	5.1	0.019	0.8	0.012
0 to 8640	5.8	0.011	0.5	0.011
0 to 10800	1.8	0.008	0.7	0.0101
0 to 12960	1.4	0.005	1.7	0.0099
0 to 15120	0.36	0.0036	1.37	0.0099
0 to 17280	0.36	0.0036	1.24	0.0099
0 to 19440	0.36	0.0036	1.26	0.0099
0 to 21600	0.36	0.0036	1.26	0.0099

We inspected the convergence of the spectral solution over those areas where the largest differences w.r.t. the numerical integration were present. Over land areas, the spectral method exhibits very slow convergence over a region bounded by 24° to 28° geocentric latitude and 81 to 85° longitude. Fig. 8 details the convergence behaviour as a function of n_{max} used in the spectral method (array of 4 x 2 panels) and draws a comparison with the topography over that region (right panel). Surprisingly, the largest differences do not coincide with highest or roughest topography, but occur in the vicinity, over smooth and low-lying terrain (compare gravity differences with topographic heights in Fig. 8). Even for n_{max} = 10,800 and 12,960, the maximum differences between gravity from both methods exceed the 1 mGal level. The associated error patterns (a result of the truncation of the spectral model) bear resemblance with a "fan", the amplitudes of which reduce with increasing n_{max}. They finally disappear when the spectral modelling is extended to n_{max} = 17,280 (cf. Fig. 8), leaving numerical integration errors of ~0.1-0.2 mGal amplitude as the governing source of discrepancies.

Over the ocean areas, spuriously large gravity differences were detected near Kiribati (Oceania) at 1°S latitude and 168°W longitude (Figure 9) above an ocean trench. Over that area, the agreement between gravity from both methods is excellent for $n_{max} \in$ [4,320 6,480 8640] (discrepancies are well below the mGal-level), but deteriorates for higher harmonic degrees. From Fig. 9, error patterns of ~1-2 mGal amplitude build up over the ocean trench when n_{max} is extended to 10,800 or higher (computation points in both methods are located at $H = 0$). We interpret this behaviour as divergence in spectral forward modelling, which emerges as the gravity modelling is extended to ultra-high degree, in our case beyond degree ~8,640 (also see histograms of differences in Fig. 10). With ~1.70 mGal, the amplitude of the error pattern is largest for n_{max} = 12,960 (Fig. 9 and Table 3), but reduces to ~1.26 mGal for n_{max} = 21,600.
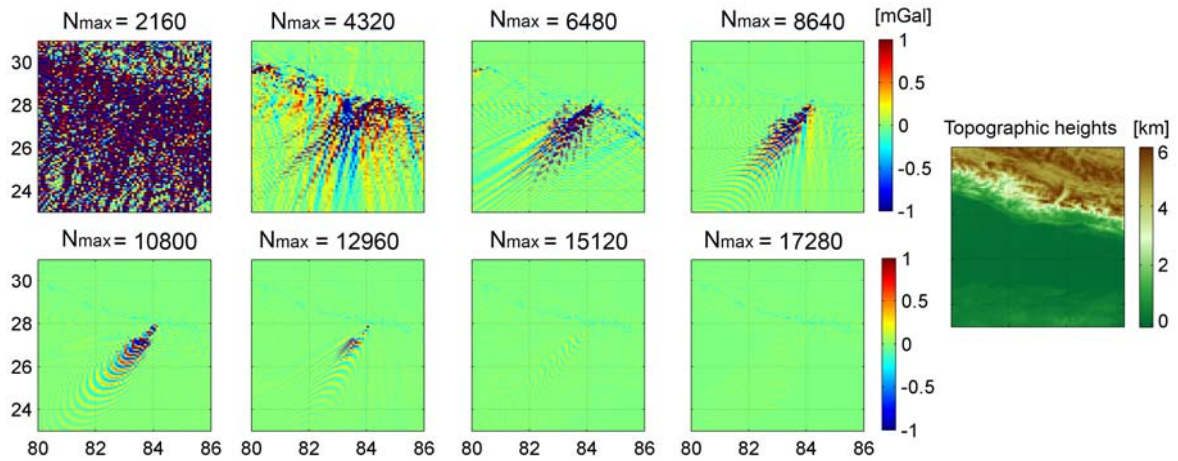
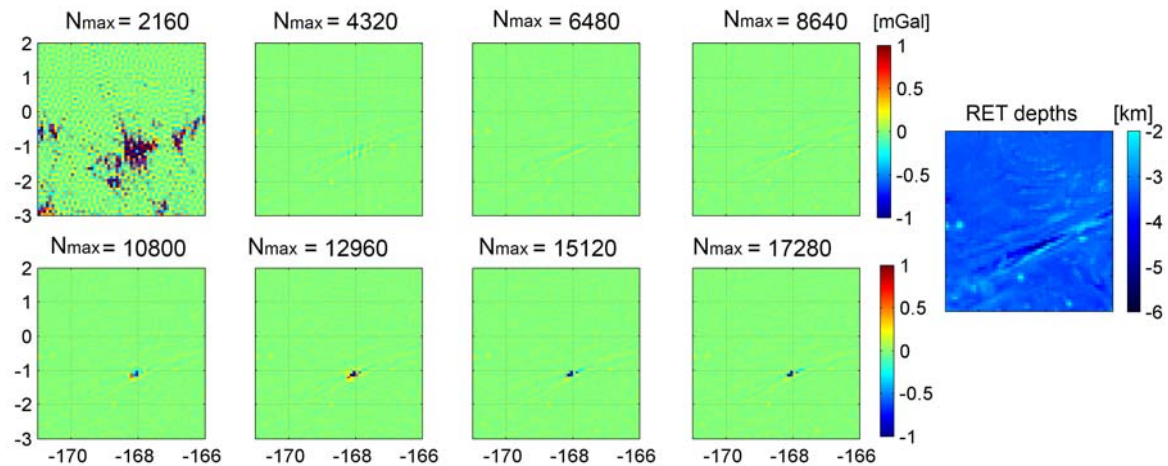**Figure 8.** Fan effect in spectral forward modelling: Gravity differences "spectral method minus Newtonian integration" as a function of the maximum degree N_{max} considered in the spectral modelling, unit in mGal. Differences are shown for 8 different N_{max} (2160 to 17,280) over area bounded by 23 to 31° geocentric latitude and 80 to 86° longitude. For comparison purposes, topographic heights (from the degree-2160 RET2012 model) are shown on the right side over the same area, unit in km. The figure shows an area of rather slow convergence near rugged topography.

Figure 9. Divergence in spectral forward modelling: Gravity differences spectral method minus Newtonian integration as a function of the maximum degree N_{max} considered in the spectral modelling, unit in mGal. Differences are shown for 8 different N_{max} (2160 to 17,280) over area bounded by -3 to 2° geocentric latitude and -171 to -166° longitude. For comparison purposes, bathymetric (RET) depths (from the degree-2160 RET2012 model) are shown on the right side over the same area, unit in km. The figure shows an area of moderate divergence over deep bathymetry that is related to the multiples of the input-bandwidth in the spectral method.

The histograms of gravity differences (Fig. 10) and statistics (Table 3) clearly suggest that there are no areas of divergence over the world's oceans when the spectral model is extended to $n_{max} = 8640$ (magnitude of all differences are always smaller than 0.5 mGal). For land areas, the best agreement between both methods is achieved for all $15,120 \leq n_{max} \leq 21,600$. While the

convergence is rather slow near rugged mountain areas (e.g., Fig. 8), there is no indication of divergence at all over land areas (Fig. 10, bottom row).
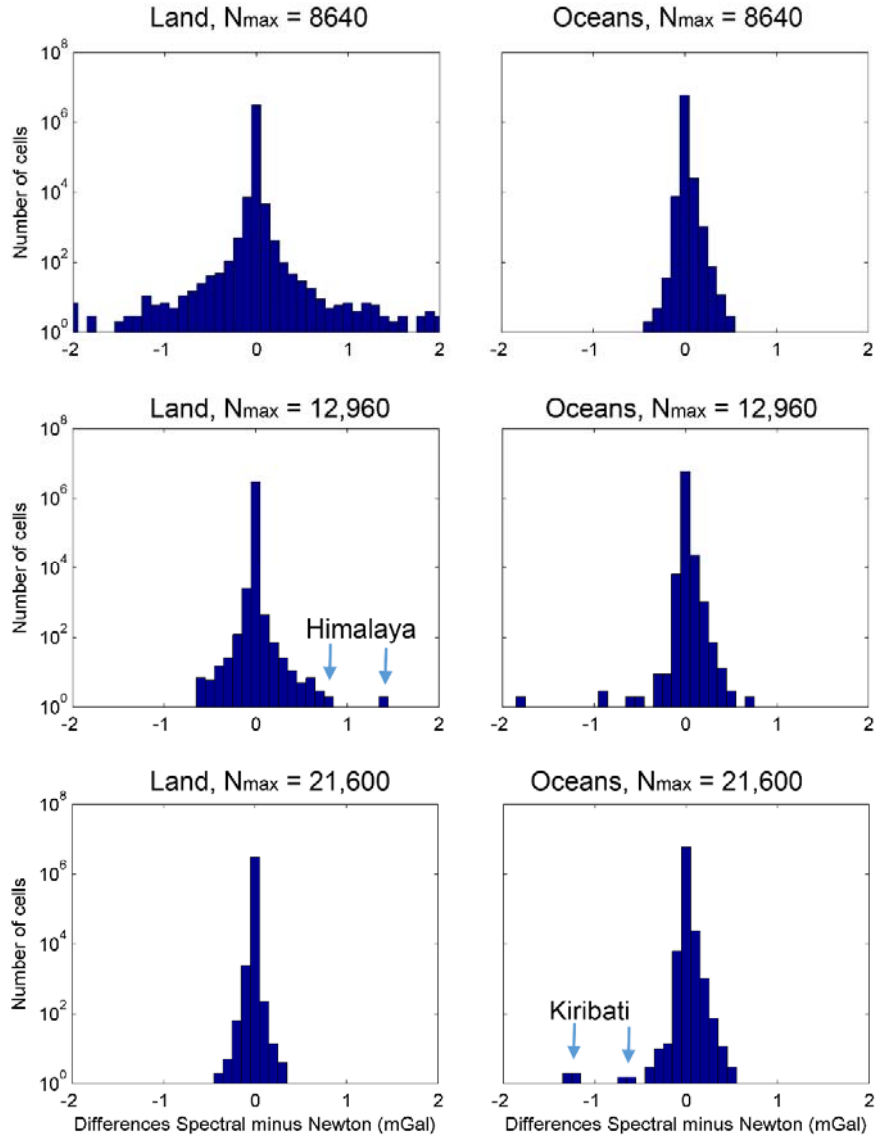

Figure 10. Histograms of gravity disturbance differences "spectral forward modelling minus Newtonian integration", reported for land areas (left column) and ocean areas (right column) for truncations $N_{max} = 8{,}640$ (top row), $N_{max} = 12{,}960$ (middle) and $N_{max} = 21{,}600$ (bottom row). Unit in mGal, class width 0.1 mGal in all cases.

6. Discussion

We have cross-validated topographic gravity - as implied by a degree-2160 topographic mass model - using two independent gravity forward modelling techniques. Our global validation experiment (Sect. 5.3) revealed an agreement between gravity from both methods over land areas at the ~4 µGal-level, with the maximum discrepancies always smaller than 0.5 mGal. Over the

oceans, the RMS-agreement was found to be at the ~10 µGal level (RMS), with maximum discrepancies exceeding the 1 mGal threshold only for two cells near Kiribati (Fig. 10), close to a deep ocean trench. Given these discrepancies reduce to 0.5 mGal, when the spectral modelling is limited to $n_{max} = 8,640$, it is reasonable to conclude that both methods are suitable for gravity modelling over the oceans too. Overall, the agreement can be considered very good, providing a satisfactory check on (a) the Newton integration with discretized mass-elements, and (b) the convergence of the spherical-harmonic series expansion of the topographic potential over most of the globe.

The local validation experiment (Sec. 5.2) demonstrated that the aforementioned discrepancies are primarily due to discretisation errors of the mass model in the numerical integration. Higher oversampling of the mass model (near the computation points) would – without doubt – further improve the agreement with the spectral method and certainly reduce many of the ~0.2 mGal discrepancies over steep terrain (cf. evidence in Fig. 4c and 4d). This, however, is not required in view of most practical applications and little justifiable in view of the massive additional computational resources required compared to those already used (cf. Table 1).

Contrary to our initial expectation, the area chosen for the local experiment (rugged topography including the Mount Everest) did not serve well as a worst-case scenario for modelling errors. It was only through the global experiment that areas of largest discrepancies could be detected and investigated (Figures 8 and 9). This demonstrates that largest modelling errors do not necessarily occur over areas of roughest topography, but – as in our example – over flat terrain near the high mountains, and over one (but not the deepest) of the ocean trenches. As important lesson learned, global validation experiments cannot be reliably substituted through – even thoughtfully selected – local test areas.

Our numerical study has shown that the topographic gravity field – as generated by a degree-2160 topographic mass model – reaches significant signal amplitudes at the 20 mGal level beyond degree 2160, while its power is negligible beyond degree ~17,280. In terms of maximum signals, about ~90% of this short-scale spectral energy is concentrated in the second multiple of the input band (degrees 2161-4320), another ~8 % in the third multiple, and the remainder beyond harmonic degree 6480. The consideration of these short-scale signals is important in any comparison against Newtonian integration. This is because the numerical integration inherently delivers spectrally complete gravity effects, and spectral consistency is mandatory for meaningful cross-comparisons between the two forward techniques [*Hirt and Kuhn,* 2014].

As a side note, our numerical comparisons revealed the importance of the higher-order powers of the topographic height function up to integer power 13, when a complete gravity field model of a degree-2160 Earth topography is to be computed. This augments previous studies by *Hirt and Kuhn* [2014] who demonstrated the relevance of integer powers of 6 (for a gravity model to degree 2160 generated by a degree-360 topography), and *Chambat and Vallete* [2005], who showed the significance of integer power 2 (using a degree 360 topography and comparisons against EGM96).

The gravity field of Earth's topography was forward-modelled in spherical approximation (i.e. Earth approximated as a mass-sphere and topography mapped onto the surface of that sphere) and not in the more advanced ellipsoidal approximation (i.e. forward modelling w.r.t. mass ellipsoid and no mapping). Given that the differences between topographic gravity from both levels of approximation are very small (for degree-2160 models: maximum difference less than 5 mGal, RMS about 1.2 mGal, cf. *Claessens and Hirt* [2013]), our study makes an indirect contribution towards the validation of topographic gravity modelling in ellipsoidal approximation too. Notwithstanding, a direct validation of topographic gravity modelling in ellipsoidal approximation is considered important and possible with a similar methodology.

7. Conclusions

As the key conclusion of this paper, all series expansions involved in the spectral forward modelling technique could be shown to sufficiently converge for a degree-2160 Earth topography model over most of Earth's surface. As such, evidence is obtained that the spectral forward modelling technique is suitable for modelling of Earth's topographic potential from degree-2160 topographies in spherical harmonics, and, thus, accurate construction of global Bouguer gravity maps with 10 km resolution. The divergence effect detected near Kiribati occurred for ultra-high degrees, beyond degree 8,640 only, so is not a critical effect for Bouguer gravity maps that are band-limited to degree 2,160.

With a maximum harmonic degree of 2,160 (~10 km in North-South direction), the spectral band-width of our topography model was chosen commensurate with those of modern geopotential models such as EGM2008 [*Pavlis et al.,* 2012] or models from the EIGEN initiative [*Förste et al.,* 2014]. In view of global Bouguer gravity maps from these GGMs, our study shows a more than adequate precision for the computation of the topographic gravity component. As a central outcome, large discrepancies of several 10s of mGal between topographic gravity computations, as reported in other studies [e.g., *Yang et al.,* 2010], are not a concern for modern degree-2160 Bouguer gravity maps (constructed with the methods described in our paper). There is little doubt that the discrepancies reported in *Balmino et al.* [2012] and *Yang et al.* [2010] are (at least partially) explained due to not modelling the short-scale gravity signals beyond the bandwidth of the input topography in the spectral method.

Crucial to the success of the cross-validation was the expansion of the topographic potential into multiple integer powers of the topographic height function and, most importantly, explicit modelling of the short-scale signals much beyond the spectral resolution of the input topography model. Starting from a degree-2160 model of Earth's topography, we modelled the contributions of its integer powers to the implied topographic potential to power 15 and short-scale gravitational signals to ultra-high degree of 21,600, yielding a very complete spectral model of the topographic potential generated by our band-limited topography. To our knowledge, a similarly high-resolution topographic gravity modelling effort has not been presented before. This may also be related to the significant computational expenses related to Newtonian integration and to spectral forward

modelling, where multiple SHA to ultra-high degree were required to construct a widely complete spectral model of the implied gravity field.

As future work, a detailed examination of the convergence and accuracy of the spectral forward method is required for degree-10800 topography, as already used in the context of UNESCO's WGM2012 world gravity mapping [*Bonvalot et al.,* 2012]. This, however, is deemed to be computationally extraordinarily challenging, given the necessities to model short-scale signals down to sub-km scales in spherical harmonics (or multiples of degree 10,800), and several higher-order integer powers of the topographic mass model.

Acknowledgements

Literature

Amante, C., and B.W. Eakins (2009), ETOPO1 1 arc-minute global relief model: Procedures, Data Sources and Analysis, *NOAA Technical Memorandum* NESDIS NGDC-24, 19 p.

Anderson, E.G. (1976), The effect of topography on solutions of Stokes' problem. Unisurv S-14 Report, *School of Surveying*, University of New South Wales, Kensington.

Balmino, G. (1994), Gravitational potential harmonics from the shape of a homogenous body. *Celestial Mechanics and Dynamic Astronomy* 60, 331-364.

Balmino, G., N. Vales, S. Bonvalot and A. Briais (2012), Spherical harmonic modelling to ultra-high degree of Bouguer and isostatic anomalies*, J. Geod.,* 86(7), 499-520, doi: 10.1007/s00190-011-0533-4.

Becker, J.J., D.T. Sandwell, W.H.F. Smith, J. Braud, B. Binder, J. Depner, D. Fabre, J. Factor, S. Ingalls, S-H. Kim, R. Ladner, K. Marks, S. Nelson, A. Pharaoh, R. Trimmer, J. Von Rosenberg, G. Wallace and P. Weatherall. 2009. Global Bathymetry and Elevation Data at 30 Arc Seconds Resolution: SRTM30_PLUS. *Marine Geod.* 32(4): 355-371.

Braitenberg C, C. Hirt, B. Bucha, (2015), Global Gravity Maps in Support to Geothermal Energy Sourcing. New Earth Bouguer Gravity map as layer in the IRENA Global Atlas International Renewable Energy Agency (irena.org) http://irena.masdar.ac.ae/?map=1046

Bonvalot, S., Balmino, G., Briais, A., Kuhn, M., Peyrefitte, A., Vales, N., et al. (2012), World Gravity Map, 1:50,000,000 map, Eds.: BGI-CGMW-CNES-IRD, Paris.

Bucha, B. and Janák, J. (2014), A MATLAB-based graphical user interface program for computing functionals of the geopotential up to ultra-high degrees and orders: Efficient computation at irregular surfaces, *Comp. and Geosci.*, 66, 219-227, doi: 10.1016/j.cageo.2014.02.005.

Cella, F. (2015) GTeC — A versatile MATLAB® tool for a detailed computation of the terrain correction and Bouguer gravity anomalies, *Comp. and Geosci.*, 84, 72-85, doi:10.1016/j.cageo.2015.07.015

Chambat, F., and B. Valette (2005), Earth gravity up to second order in topography and density, *Physics Earth Plan. Int.,* 151 (1-2) 89-106, doi:10.1016/j.pepi.2005.01.002.

Chao, B.F. and D.P. Rubincam (1989), The gravitational field of Phobos. Geophysical Research Letters 16(8), 859-862.

Claessens S.J. and C. Hirt (2013), Ellipsoidal topographic potential - new solutions for spectral forward gravity modelling of topography with respect to a reference ellipsoid*, J. Geophys. Res.,* 118(11), 5991-6002, doi: 10.1002/2013JB010457.

Forsberg R. (1984), A study of terrain reductions, density anomalies and geophysical inversion methods in gravity field modelling. *Report* 355, Department of Geodetic Science and Surveying, Ohio State University, Columbus.

Förste, C., Bruinsma, S.L., Abrikosov, O., Lemoine, J.-M. Marty, Jean, C., Flechtner, F., Balmino, G. Barthelmes, F.; Biancale, R. (2014), EIGEN-6C4 The latest combined global gravity field model including GOCE data up to degree and order 2190 of GFZ Potsdam and GRGS Toulouse. GFZ Data Services. http://dx.doi.org/10.5880/icgem.2015.1

Fukushima T. (2012), Numerical computation of spherical harmonics of arbitrary degree and order by extending exponent of floating point numbers. *J. Geod.,* 86(4), 271–285, doi: 10.1007/s00190-011-0519-2.

Grombein, T, K Seitz, B Heck (2016), The Rock–Water–Ice Topographic Gravity Field Model RWI_TOPO_2015 and Its Comparison to a Conventional Rock-Equivalent Version, *Surv. Geophys.* 37(5), 937-976, doi:10.1007/s10712-016-9376-0.

Gruber C., Novák P., F. Flechtner and F. Barthelmes (2014), Derivation of the topographic potential from global DEM models, *International Association of Geodesy Symposia* 139, Springer-Verlag Berlin Heidelberg, 535-542, doi: 10.1007/978-3-642-37222-3__71.

Grüninger, W. (1990), Zur topographisch-isostatischen Reduktion der Schwere. *PhD Thesis*, Universität Karlsruhe.

Hammer, S. (1939), Terrain corrections for gravimeter stations, *Geophysics* 4, 184-194.

Hirt, C. (2012), Efficient and accurate high-degree spherical harmonic synthesis of gravity field functionals at the Earth's surface using the gradient approach, *J Geod.,* 86(9), 729-744, doi:10.1007/s00190-012-0550-y.

Hirt, C., M. Kuhn (2012), Evaluation of high-degree series expansions of the topographic potential to higher-order powers*, J. Geophys. Res.,* 117, B12407, doi:10.1029/2012JB009492.

Hirt, C. (2013), RTM gravity forward-modelling using topography/bathymetry data to improve high-degree global geopotential models in the coastal zone, *Marine Geod.,* 36(2), 1-20, doi:10.1080/01490419.2013.779334.

Hirt, C., Kuhn, M. (2014), Band-limited topographic mass distribution generates full-spectrum gravity field: Gravity forward modeling in the spectral and spatial domains revisited *J. Geophys. Res.,* 119(4), 3646-3661.

Hirt, C., Rexer M (2015), Earth 2014: 1' shape, topography, bedrock and ice-sheet models—available as gridded data and degree 10,800 spherical harmonics. *Int J Appl Earth Obs Geoinf* 39:103–112. doi:10.1016/j.jag.2015.03.001.

Heck, B., and K. Seitz (2007), A comparison of the tesseroid, prism and point-mass approaches for mass reductions in gravity field modelling. *J Geod.,* 81(2), 121-136, doi: 10.1007/s00190-006-0094-0.

Hwang, C., C-G. Wang, Y-S Hsiao (2003), Terrain correction computation using Gaussian quadrature, *Comp. and Geosci.*, 29, 1259-1268.

Jacoby, W., and P.L. Smilde (2009), *Gravity interpretation,* Springer, Berlin, Heidelberg

Jarvis, A., H.I. Reuter, A. Nelson, and E. Guevara (2008), Hole-filled SRTM for the globe Version 4, Available from the CGIAR-SXI SRTM 90m database. Available at: http://srtm.csi.cgiar.org.

Jekeli, C., J.K. Lee and J.H. Kwon (2007), On the computation and approximation of ultra-high-degree spherical harmonic series. *J Geod.,* 81(9), 603-615, doi 10.1007/s00190-006-0123-z.

Kuhn, M. (2000), Geoidbestimmung unter Verwendung verschiedener Dichtehypothesen, Reihe C, Heft Nr. 520. *Deutsche Geodätische Kommission*, München.

Kuhn, M. (2003), Geoid determination with density hypotheses from isostatic models and geological information. *J. Geod.* 77(1–2):50–65

Kuhn, M., and K. Seitz (2005), Comparison of Newton's Integral in the Space and Frequency Domains, in *A Window on the Future of Geodesy*, IAG Symposia vol. 128, ed F Sanso, 386-391, Springer, Berlin, Heidelberg.

Kuhn, M., W.E. Featherstone, and J.F. Kirby (2009), Complete spherical Bouguer gravity anomalies over Australia, *Australian J. Earth Sci.,* 56, 213-223.

Kuhn, M., and C. Hirt (2016), Topographic gravitational potential up to second-order derivatives: an examination of approximation errors caused by rock-equivalent topography (RET); *J. Geod.,* 90(9), 883-902,10.1007/s00190-016-0917-6.

Mader, K. (1951), Das Newtonsche Raumpotential prismatischer Körper und seine Ableitungen bis zur dritten Ordnung. *Österreichische Zeitschrift für Vermessungswesen*, Sonderheft 11, Wien.

Nagy, D., G. Papp, and J. Benedek (2000), The gravitational potential and its derivatives for the prism. *J. Geod.* 74(7), 552-560, Erratum in *J. Geod.,* 76(8):475.

Nahavandchi, H. (1999), Terrain correction computations by spherical harmonics and integral formulas, *Physics and Chemestry of the Earth part A* 24(1), 73-78.

Nowell, D.A.G. (1999), Gravity terrain corrections – an overview, *Journal of Applied Geophysics* 42, 117-134.

Pail, R., S. Bruinsma, F. Migliaccio, C. Förste, H. Goiginger, W.-D. Schuh, E. Höck, M. Reguzzoni, J.M. Brockmann, O. Abrikosov, M. Veicherts, T. Fecher, R. Mayrhofer, I. Krasbutter, F. Sansò, and C.C. Tscherning (2011), First GOCE gravity field models derived by three different approaches, *J Geod.,* 85(11), 819-843, doi: 10.1007/s00190-011-0467-x.

Pavlis N.K., S.A. Holmes, S.C. Kenyon, and J.K. Factor (2008), An Earth Gravitational Model to Degree 2160: EGM2008, Presented at the 2008 General Assembly of the European Geoscience Union, Vienna, Austria, April 13-18, 2008.

Pavlis, N.K., Holmes, S.A., Kenyon, S.C., Factor, J.K. (2012) The development and evaluation of the Earth Gravitational Model 2008 (EGM2008), *J. Geophys. Res.,* 117, B04406, DOI: 10.1029/2011JB008916

Rexer, M. and C. Hirt (2015), Ultra-high degree surface spherical harmonic analysis using the Gauss-Legendre and the Driscoll/Healy quadrature theorem and application to planetary topography models of Earth, Moon and Mars. *Surveys in Geophysics* 36(6), 803-830, doi:10.1007/s10712-015-9345-z.

Rexer, M., C. Hirt, S. Claessens, and C. Braitenberg (2015), Use of topography in the context of the GOCE satellite mission - some examples. In: *Proceedings of 5th International GOCE User Workshop*, Paris, France, published in European Space Agency (ESA) SP-728, March 2015.

Rexer, M., C. Hirt, S.J. Claessens and R. Tenzer (2016), Layer-based modelling of the Earth's gravitational potential up to 10km-scale in spherical harmonics in spherical and ellipsoidal approximation, Surv. Geophys., doi: 10.1007/s10712-016-9382-2.

Rummel, R., R.H. Rapp, H. Sünkel, and C.C. Tscherning (1988), Comparisons of global topographic/isostatic models to the Earth's observed gravity field, Report No 388, *Dep. Geodetic Sci. Surv.,* Ohio State University, Columbus, Ohio.

Tenzer, R. (2005), Spectral domain of Newton's integral, *Boll Geod. Sci. Affini,* 2, 61-73.

Tenzer R., A. Abdalla, P. Vajda, Hamayun (2010), The spherical harmonic representation of the gravitational field quantities generated by the ice density contrast. *Contrib Geophys Geod* 40(3):207–223.

Tsoulis, D., P. Novák, and M. Kadlec (2009), Evaluation of precise terrain effects using high-resolution digital elevation, models, *J. Geophys. Res.,* 114, B02404, doi:10.1029/2008JB005639.

Vaniček, P., Novák, P., Martinec, Z. (2001), Geoid, topography, and the Bouguer plate or shell, *J. Geod.,* 75(4), 210-215.

Wang, Y.M., S. Holmes, J. Saleh, X.P. Li and D. Roman (2010), A comparison of topographic effect by Newton's integral and high degree spherical harmonic expansion – Preliminary Results, poster presented at WPGM 2010 Taipei, Taiwan, June 22 -25

Watters, T.R., McGovern, P.R., R.P. Irwin III (2007), Hemispheres Apart: The Crustal Dichotomy on Mars. *Annu. Rev. Earth Planet. Sci.* 2007. 35:621–52, doi: 10.1146/annurev.earth.35.031306.140220.

Wieczorek, M.A., and R.J. Phillips (1998), Potential anomalies on the sphere: Applications to the thickness of the lunar crust, *J. Geophys. Res.,* 103(E1), 1715-1724, doi:10.1029/97JE03136.

Wieczorek, M.A. (2007), The gravity and topography of the terrestrial planets, In: Schubert G (ed) *Treatise on Geophysics,* 10, 165-206, Elsevier-Pergamon, Oxford, U.K.

Wieczorek, M.A. (2015), Gravity and Topography of the Terrestrial Planets. In: Schubert G (ed) *Treatise on Geophysics*, 2nd edition, Oxford, 153-193, doi:10.1016/B978-0-444-53802-4.00169-X, 2015.

Zuber, M.T., D.E. Smith et al. (2012), Gravity Field of the Moon from the Gravity Recovery and Interior Laboratory (GRAIL) Mission, *Science,* 5 December 2012, doi. 10.1126/science.1231507.